

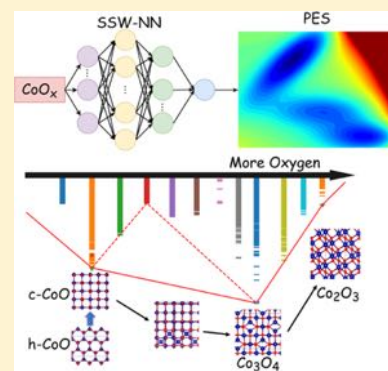
Stability and Phase Transition of Cobalt Oxide Phases by Machine Learning Global Potential Energy Surface

Fan-Chen Kong, Ye-Fei Li,[✉] Cheng Shang,[✉] and Zhi-Pan Liu*[✉]

Collaborative Innovation Center of Chemistry for Energy Material, Key Laboratory of Computational Physical Science (Ministry of Education), Shanghai Key Laboratory of Molecular Catalysis and Innovative Materials, Department of Chemistry, Fudan University, Shanghai 200433, China

Supporting Information

ABSTRACT: Cobalt oxides (CoO_x), despite its wide applications, are notoriously complex on structure, in particular under experimental reduction/oxidation conditions. Here, using the newly developed machine learning method, stochastic surface walking global optimization in combination with global neural network potential, we are able to, for the first time, explore the global potential energy surface (PES) of CoO_x at different Co/O ratios. Rich information on the thermodynamics and kinetics of CoO_x is thus gleaned from more than 10^7 PES data, which helps to resolve the long-standing puzzles on CoO_x chemistry. We show that (i) only CoO and Co_3O_4 are thermodynamically stable compositions in CoO_x , whereas Co_3O_4 is the most stable phase. The trivalent Co_2O_3 , although having a well-defined global minimum, tends to decompose to Co_3O_4 and O_2 at finite temperatures. (ii) The solid phase transition between wurtzite CoO (h-CoO) and rock salt CoO (c-CoO) follows the reconstructive phase transition mechanism with a high barrier. Because a high temperature is required for transition, the strong preference of structural defects inside c-CoO instead of h-CoO contributes to the one-way solid-phase transition from h-CoO to c-CoO. (iii) It is c-CoO that can achieve a coherent interface with Co_3O_4 in forming a biphasic junction, which implies the reversibility of Co_3O_4 and c-CoO transition under reduction/oxidation conditions. Our results demonstrate the power of global neural network potential in material discovery for fast exploration of polymorphism and transition kinetics and lay the structural foundation for understanding CoO_x applications.



1. INTRODUCTION

Cobalt oxides (CoO_x) with their versatile oxidation states and geometrical structures are of wide applications. Unlike many common oxides (e.g., TiO_2), cobalt oxides are often utilized as a solid mixture with different Co oxidation states and coordinations. For instance, in a Co-based Fischer–Tropsch catalyst,^{1–3} a variety of oxidized Co forms, including tetrahedral coordinated Co^{2+} , octahedral Co^{2+} , and octahedral Co^{3+} atoms, are identified in reaction. It is now a general consensus that the polymorphism of CoO_x is sensitive to the thermodynamic relative stability of the $\text{Co}^0/\text{Co}^{2+}/\text{Co}^{3+}$ oxidation states under different synthetic conditions, that is, oxidizing or reducing atmosphere, most likely because of the relatively flat potential energy surface (PES) between different CoO_x phases. It remains highly challenging to understand the properties of CoO_x , which requires detailed knowledge of their atomic structures at different chemical compositions, including both crystal forms and possible phase junctions.

To date, only three cobalt oxide crystal structures are well characterized under ambient conditions: (i) Rock salt monoxide (c-CoO, $Fm\bar{3}m$, #225), (ii) hexagonal monoxide CoO (h-CoO, $P6_3mc$, #186), and (iii) spinel Co_3O_4 ($Fd\bar{3}m$, #227) with mixed valency (Co^{2+} and Co^{3+}). Rock salt c-CoO has a single type of Co^{2+} octahedrally coordinated ($[\text{CoO}_6]$) with lattice oxygen in a $Fm\bar{3}m$ symmetry. Hexagonal h-CoO is composed by tetrahedral

coordinated Co^{2+} ($[\text{CoO}_4]$) with a wurtzite structure (similar to ZnS and CdSe). Co_3O_4 has a spinel structure, where the O anions form a cubic close-packing array, one-eighth of tetrahedral interstices are occupied by high-spin Co^{2+} ions, and one-half of octahedral interstices are occupied by low-spin Co^{3+} ions.

Experiments have shown that different crystal phases can be prepared by exploiting their mutual transformation by controlling reaction conditions. Starting from $\text{Co}(\text{acac})_3$ (acac = acetylacetonate), hexagonal CoO (h-CoO) can be selectively prepared at high temperature (185 °C) and with a short time (2 h), whereas the lower temperature (130 °C) and longer reaction time (12 h) will form c-CoO.^{4,5} A crystal-to-crystal phase transition is observed from h-CoO to c-CoO under heating to 320 °C (either under vacuum or in an inert atmosphere) or at the high pressure (0.8–6.0 GPa at ambient temperature).⁶ Both c-CoO and h-CoO will be oxidized to Co_3O_4 when annealed at 240 °C under atmospheric pressure of air.⁵ During the oxidation, h-CoO converts to Co_3O_4 by a phase transition to c-CoO first as proved by X-ray diffraction. Co_3O_4 can be reduced by hydrogen above 291 °C to c-CoO.⁷

Received: March 26, 2019

Revised: May 22, 2019

Published: June 26, 2019

Because of the solid-to-solid transitions between phases, the change of the oxidation state and the coordination for Co atoms are rather common in Co-based materials/catalysts, leading to a great difficulty in characterizing the properties of CoO_x . To date, many important questions on CoO_x phases remain open. Two of them are elaborated below.

- (i) The solid-phase transition mechanism between common CoO_x phases, in particular, the CoO phase transition between c-CoO and h-CoO. Because h-CoO and c-CoO stand for two key coordination statuses of Co atoms ($[\text{CoO}_4]$ and $[\text{CoO}_6]$ as mentioned above), the phase transition between them can largely determine the ratio of tetrahedral to octahedral Co atoms in CoO_x , which is a key measure to characterize CoO_x and correlate with the properties. Experimentally, h-CoO can transform to c-CoO, not the vice versa. This one-way phase transition is in sharp contrast to the reversible Co_3O_4 to c-CoO transition under reduction/oxidation conditions.
- (ii) The most stable phase of CoO_x at different chemical compositions, in particular, the trivalent oxide Co_2O_3 . Despite some claims to give Co_2O_3 in nanocrystal synthesis,⁸ its most stable crystal form under ambient condition has not been reported yet. The presence of Co_2O_3 in CoO_x nanocrystals can be characterized by electron diffraction but is not seen from X-ray powder diffraction. Co_2O_3 is also reported as a component in CoO_xH_y mixtures, such as $\text{CoO}-\text{Co}_2\text{O}_3-\text{Co}(\text{OH})_2$ nanoparticles in Co-based electrochemical catalysts, as deduced from X-ray absorption near-edge structure.⁹ Nevertheless, crystalline Co_2O_3 at high pressure (9 GPa) can be produced with a corundum-type (Al_2O_3) structure ($R\bar{3}c$, #167), where Co is suggested at the low spin state.¹⁰

Obviously, the answer to the above questions would help to resolve the atomic structure of CoO_x under reaction conditions and thus guide the controlled synthesis on CoO_x . In this work, we aim to shed light into the microstructure of CoO_x phases using the newly developed SSW-NN method,^{11,12} that is, the stochastic surface walking (SSW) global sampling^{13,14} in combination with the global neural network (G-NN) potential. For the first time, the global PES of cobalt oxide with different oxygen atomic contents (O%: 0.49–0.60, corresponding to Co oxidation state from 2+ to 3+) have been explored, which leads to the identification of the most stable phase, the so-called global minimum (GM), for each composition and the establishment of the thermodynamic convex hull diagram for CoO_x . With these large data from global PES, we resolve some key puzzles on the thermodynamics and kinetics of CoO_x , such as CoO solid-phase transition and Co_2O_3 stability.

2. METHODS

2.1. SSW Global Optimization and Pathway Sampling.

The SSW global optimization method^{13,14} as implemented in LASP code developed in the group¹⁵ is utilized to sample the global PES of CoO_x at each selected composition. SSW method features with the soft movement on PES as guided by the random soft mode (second derivative) direction, which is capable to explore both minima and transition states (TSs) on global PES with high efficiency. By combining SSW with the efficient global NN potential (described below), we are able to tackle complex PES problems, ranging from the thermodynamic phase diagram to the solid-phase transition.

The solid-phase transition mechanism between h-CoO and c-CoO has been investigated using SSW-based reaction sampling (SSW-RS)¹⁶ method to sample exhaustively the possible pathways. All likely reaction pathways from SSW-RS are connected by variable-cell double-ended surface walking method,¹⁷ from which the TS and the lowest energy pathway is identified. The reaction pathways are further verified by computing the associated imaginary frequency and extrapolating TS structures toward initial state (IS) and final state (FS). The convergence criteria for all the structures are the maximum atomic force component below 0.01 eV/Å and stress below 0.01 GPa. More details on the SSW and SSW-RS method can be found in the Supporting Information and also in our previous work.^{16,17}

2.2. CoO_x G-NN Potential.

The G-NN potential is generated using the SSW-NN method^{11,12} now built in LASP code.¹⁵ The G-NN potential is trained using the first-principles density functional theory (DFT, see 2.3 for details) data set by minimizing the difference between NN and DFT results on the total energy, force, and stress. The first-principles data set is obtained iteratively by learning the SSW global PES that covers a wide range of CoO_x compositions. In each cycle, the G-NN potential is tested with newly generated structures from SSW. More than 10^7 structures on CoO_x PES were visited by SSW-NN during NN potential generation and the final training data set of CoO_x consists of 42 246 structures to represent different chemical environments, ranging from cluster, bulk, to layers/surfaces (see Supporting Information Table S1) and covering a wide range of chemical compositions for CoO_x from Co/O ~1:1 to Co/O ~2:3 (see the Supporting Information 1.1.a). For the final G-NN potential, the root-mean-square (rms) errors for the energy and the force reaches 12.063 meV per atom and 0.210 eV/Å, respectively. We have also benchmarked the NN calculations against DFT results for important low-energy structures, which shows that the energy rms error is 5.604 meV per atom for these important minima (see Supporting Information Section 1.1.b). This small error suggests that the NN PES is a good approximation to DFT PES of CoO_x and can be utilized to expedite the global structure search and pathway determination. It should be emphasized that the GM from NN at each composition is always further examined by DFT, and in all the cases, the GM from NN remains to be the most stable structure in DFT (Table S2). All structures reported in this work, including those in pathways and low-energy structures for each composition, are discovered by SSW-NN simulation and then calculated by DFT calculations. Without explicitly mentioning, all reported energetics are based on DFT calculations.

2.3. DFT Calculations for CoO_x .

All first-principles DFT calculations are performed with the plane-wave VASP package^{18,19} using projector-augmented wave potential to describe the core electron (for other details, see the Supporting Information). Because of the strong correlation nature of CoO_x , it is known that the standard pure DFT functionals fail to describe properly the energetics and the other electronic structure properties. Table 1 lists our initial benchmarking results for two lowest energy phases of CoO, including h-CoO and c-CoO, calculated using different DFT functionals, namely generalized gradient approximation (GGA)–Perdew, Burke, and Ernzerhof (PBE),^{20–23} GGA with the Hubbard term correction for on-site Coulomb interaction (PBE + U),^{23–25} $U = 3.5$ eV for Co 3d states) and the hybrid functional HSE06. The sensitivity of U value on Co^{2+} and Co^{3+} oxides has been

Table 1. Relative Energy (in meV/Atom) and Band Gap (in eV) of CoO Phases from DFT Calculations with Different Functionals (PBE + U with $U = 3.5$ eV for Co)^c

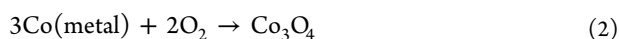
| | PBE | | PBE + U | | HSE06 | |
|--------------------|-----------------|------------------|-----------|------|-------|-----|
| | FM ^a | AFM ^a | FM | AFM | FM | AFM |
| | Relative Energy | | | | | |
| c-CoO | 146 | 52.3 | 56.0 | 15.4 | 51.3 | 8.2 |
| h-CoO | 56.7 | 0.0 | 12.4 | 0.0 | 8.6 | 0.0 |
| | Band Gap | | | | | |
| c-CoO ^b | 0.86 | 1.86 | 1.6 | 3.2 | 2.8 | 3.2 |
| h-CoO ^b | 0.25 | 0.25 | 0.6 | 1.2 | 1.8 | 2.3 |

^aFM: ferromagnetic state with the magnetic momentum being +3 for each Co and 0 for O atoms; AFM: antiferromagnetic state with ± 3 for Co atoms and 0 for O atoms (G-type AFM for c-CoO,³⁰ AFM along the c -axis for h-CoO³¹). ^bc-CoO Expt. 2.50 eV;³² h-CoO Expt. 1.60 eV.³³ ^cSee Supporting Information Section 2.1 for a detailed band structure.

benchmarked with lattice parameters and formation energy of CoO_x. A similar choice of U value for CoO_x system (in CoO, Co₃O₄ and Co₂O₃) can also be found in the work by Singh and Major,²⁶ Garcia-Mota et al.,²⁷ and Wang et al.²⁸ (also see the Supporting Information Section 1.4 for more details).^{29–33}

From the results in Table 1,³⁰ we can see that PBE + U and Heyd–Scuseria–Ernzerhof (HSE) functionals give the same tendency for energetics; that is, the wurtzite phase h-CoO always has lower energy than the rock salt phase c-CoO, and the antiferromagnetic (AFM) phase is lower than the ferromagnetic (FM) phase. The theoretical prediction for the AFM ground state agrees with the experimental measurement by Risbud et al.⁴ For PBE + U and HSE06 calculations, the energy gap between AFM c-CoO and h-CoO phases is close and much better than the PBE results. Considering that PBE + U calculations are at least 100 times more efficient than hybrid HSE06 calculations and the reasonable energetic accuracy achieved by PBE + U , we have mainly utilized the PBE + U functional in this work; that is to construct the global NN potential and to verify all the important low-energy structures for different CoO_x compositions.

Because the Hubbard U value in PBE + U calculations should in principle vary for CoO_x at different compositions, we have utilized the approach proposed by Jain et al.³⁴ to correct the energy deviation and compare different CoO_x phases. In the approach, the energetic correction corresponding to different Co/O ratios is determined by fitting a linear model between Co atomic content and the difference between experimental and DFT predicted formation enthalpy for CoO and Co₃O₄ (normalized per Co atom). The experimental data ($\Delta_f H_{\text{solid}}^0$, 298.15 K, 10⁵ Pa) for the following two chemical reactions are



−237.7 and −891 kJ/mol (−2.463, and −9.23 eV), respectively.³⁵ The linear equation fitted for the energy correction is ΔE_M (eV/atom) = 1.877 × Co % + 0.537, where Co % is the atomic content of Co in CoO_x (see Supporting Information Section 1.5 for more details).

3. RESULTS AND DISCUSSION

3.1. CoO Global PES and Solid-Phase Transition between c-CoO and h-CoO. Our investigation starts by

exploring the CoO PES using SSW-NN, where more than 40 000 minima are visited using different unit cells, mainly 16-atom and 40-atom. The other larger unit cells up to 96 atoms are also examined to confirm that there are no new local structure patterns at the low energy region. After removing the identical structural isomers, we finally obtain 6721 distinct minima, including crystals and amorphous structures.

The global PES of CoO phases are shown in Figure 1a, where the energy of the structure (eV/atom) is plotted against the

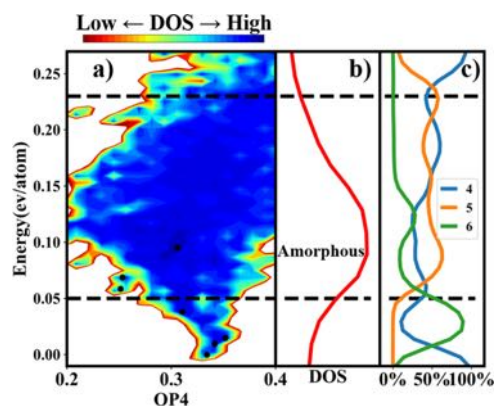


Figure 1. (a) Global PES contour plot, relative energy against the distance-weighted Steinhart-order parameter OP_4 , for CoO distinct minima sampled using minima from the SSW-NN global search; (b) DOS plot for CoO phase in (a), showing that the amorphous structures appear in the 0.05–0.23 eV/atom window; (c) percentage of different coordinated Co for CoO structures. The black dots label the representative minima shown in (a) and their coordinates (OP_4 , $E(\text{NN})$) are listed below: h-CoO (0.33, 0.000), c-CoO (0.31, 0.037), f-CoO (0.35, 0.019), CoO-Str1 (0.34, 0.008), CoO-Str2 (0.25, 0.059), CoO-Str3 (0.25, 0.069), and CoO-Str4 (0.31, 0.095). These structures are detailed in Supporting Information Section 2.2.

structural order parameter, that is the distance-weighted Steinhart-order parameter with degree $l = 4$ (OP_4) (see Supporting Information Section 1.6 for the definition of the order parameter) as utilized previously.³⁶ The contour maps for the global PES projects all the structures into a two-dimensional plot, energy and order parameter, and can show clearly the density of states (DOS) distribution for each point. The higher DOS would indicate the existence of many energetically degenerate structures with similar structure patterns, which is a typical feature for amorphous structures.

From the data set, we found that wurtzite h-CoO is the GM, where each Co atom has four neighboring O atoms including one with a relative long bond distance of 2.01 Å and three with a relative short bond distance of 1.98 Å. There are several crystal forms that nearly energetically degenerate with the GM. These structures close to GM are mainly twin or stacking faults (see Figure 1 and Supporting Information Figure S4a) of h-CoO and the zinc-blend type CoO (3.3 meV/atom, FM, $F\bar{4}3m$, #216), f-CoO. Interestingly, no stable phase junction between h-CoO and c-CoO are found from the global PES, suggesting that the two phases are difficult to grow epitaxially. On the other hand, the abundance of phase junctions between h-CoO and f-CoO in low lying structures in the global PES agrees with the experimental fact that h-CoO always coexists with f-CoO in syntheses.⁴ The c-CoO is 43.6 meV/atom (FM state) above the GM with a Co–O bond distance of around 2.14 Å. Typical structures including h-CoO, f-CoO, c-CoO, and their twin,

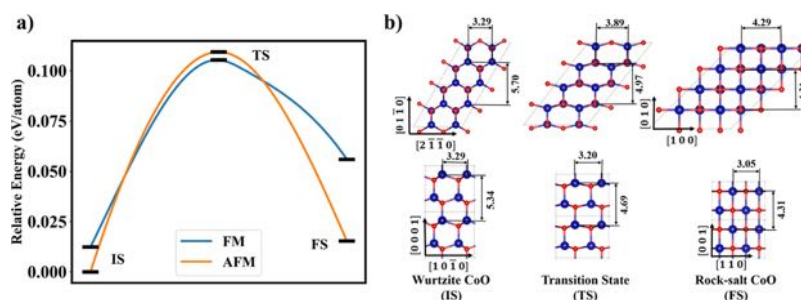


Figure 2. (a) Reaction pathway profile between h-CoO (IS) and c-CoO (FS) with FM and AFM spin states calculated from DFT PBE + U functional. (b) Snapshots for IS, TS, and FS from two different directions. Red: O atom; blue: Co atom.

stacking fault and phase junction are shown in [Supporting Information Section 2.2](#).

CoO PES enters into the amorphous zone at ~ 0.05 eV/atom above GM. There are a large number of possible minima at this energy region, which exhibit a large DOS, as shown in [Figure 1b](#). The difference between the crystal structure and amorphous structure can be better distinguished from the average Co coordination number. [Figure 1c](#) summarizes the change of different coordinated Co atoms with respect to the energy of CoO phases. We can see that there are two peaks at the low-energy region, four-coordination and six-coordination corresponding to the h-CoO-dominated and c-CoO-dominated region, respectively. By contrast, the five-coordinated Co occurs in an energy region from 0.05 to 0.27 meV/atom as the dominant coordination for the amorphous structures; six-coordination Co has the least density in the amorphous structures. A representative five-coordinated Co structure can be found in [Figure 1](#), CoO-Str4 ([Supporting Information Figure S4d](#)), where hexagonal CoO layers, such as graphene, stack together to form five-coordinated Co.

Interestingly, from the global PES structures, we now can confirm, as computed in [Table 1](#), that h-CoO is in fact energetically more stable than c-CoO, which seems to be insensitive to the DFT functionals and magnetic states. This is apparently at odds with the common knowledge from the experiment: c-CoO is often regarded as the most stable form of CoO.^{37–39} This inconsistency has also been reported recently by Saritas et al.⁴⁰ We will discuss this at the end of this section.

With the knowledge on the CoO global PES, we go further to investigate the phase transition in between h-CoO and c-CoO, which is an important phenomenon in synthesis. By using the SSW-RS method, we have sampled 10^4 reaction pathways in 16 atom unit cell, among which we identified the lowest energy reaction pathway for the transition between h-CoO and c-CoO. The energy profile of the pathway is shown in [Figure 2a](#), which has a reaction barrier of 93.0 meV/atom from PBE + U and 100.2 meV/atom from HSE06, as listed in [Table 2](#). To further confirm the results, the other larger unit cells, for example, 40-atoms and 96-atom per cell, starting from either h-CoO or c-CoO phase, have also been utilized to search for the pathway, which are found to yield the identical lowest energy pathway for the phase transition. The second lowest energy pathway has a barrier of 120.6 meV/atom, which is 16.7 meV/atom higher than the lowest energy pathway from NN PES. As shown in [Table 2](#), the reaction is little influenced by the magnetic states: the barrier is 93.0 meV/atom with FM spin and 109.4 meV/atom with the AFM spin under PBE + U . The results from HSE06 calculations again are similar to PBE + U results. We emphasize that the obtained barrier (0.1 eV/atom) for h-CoO to

Table 2. Relative Energy (meV/Atom), Volume ($\text{\AA}^3/\text{Atom}$), and Interplanar Distance (\AA) Calculated from DFT with PBE + U Functional (HSE06 Energy in Bracket)

| | c-CoO | h-CoO | TS |
|-----------------------------|-------------|-----------|---------------|
| energy (FM) | 43.6 (42.7) | 0.0 (0.0) | 93.0 (100.2) |
| energy (AFM) | 15.4 (8.23) | 0.0 (0.0) | 109.4 (115.0) |
| volume | 9.81 | 12.29 | 11.10 |
| $d(2\bar{1}10)_h, d(100)_c$ | 4.29 | 3.29 | 3.89 |
| $d(01\bar{1}0)_h, d(010)_c$ | 4.29 | 5.70 | 4.97 |
| $d(10\bar{1}0)_h, d(110)_c$ | 3.05 | 3.29 | 3.20 |
| $d(0001)_h, d(001)_c$ | 4.31 | 5.34 | 4.69 |

c-CoO is not low as the solid-phase transition occurring in bulk typically involves a significant number of atoms in lattice, for example, >10 atoms, indicating that the solid-phase transition can only occur at high temperatures.

In addition to the reaction profile, [Figure 2](#) also shows how atom moves in the phase transition from h-CoO to c-CoO via the TS. The phase transition from h-CoO to c-CoO involves a large volume reduction ($\sim 20\%$, [Table 2](#)), which is consistent with the fact that under high pressure, h-CoO can transform to c-CoO.⁴¹ From the lowest-energy pathway, we can also identify dominant lattice variation directions, that is, the expansion along $[2\bar{1}10]_h$ and the compression along $[01\bar{1}0]_h$, $[10\bar{1}0]_h$, and $[0001]_h$. After the transition, the closely packed $(0001)_h$ evolves into $(001)_c$ by compressing 19% from 5.34 to 4.31 \AA (see [Table 2](#)), and the $(2\bar{1}10)_h$ evolves into $(100)_c$ by expanding 30%, from 3.29 to 4.29 \AA (see [Table 2](#)).

With a closer inspection to the pathway, we can see that each Co atom in h-CoO evolves two additional Co–O bonds with its neighboring O atoms, changing the Co configuration from tetrahedral to octahedral coordination. From the pathway, we compute the Co atom movement distance as 1.78 \AA , which is close to a Co–O bond distance (2.14 \AA). Importantly, the phase transition involves no shearing of crystal planes, and thus, no habit plane or phase junction can be identified. The h-CoO to c-CoO solid-phase transition can be regarded as a typical reconstructive solid-phase transition.

Our finding for the reconstructive phase-transition mechanism can explain the experimental observation that the h-CoO phase transition to c-CoO involves a dramatic change in particle morphology and size. By using $\text{Co}(\text{acac})_3$ to synthesize CoO nanocrystals, Liu found that during the h-CoO transformation to c-CoO (12 h at 500 K), as the transition propagates from surface to the center of nanoparticle, h-CoO nanoparticle with a large size (~ 50 – 250 nm) breaks into a c-CoO nanoparticle with a small grain size (~ 20 nm).⁴² This fact suggests that the newly formed c-CoO can neither grow layer-by-layer nor attach strongly with the h-CoO matrix, consistent with the

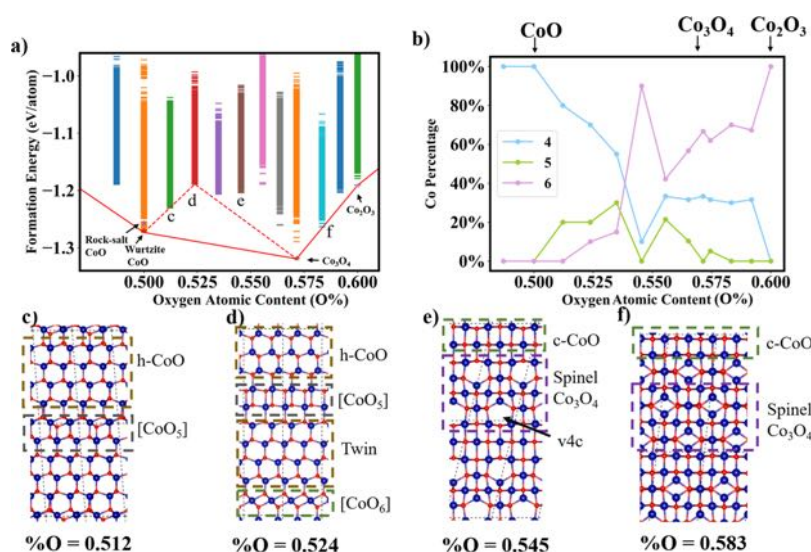


Figure 3. (a) Thermodynamic convex hull diagram for CoO_x with respect to Co metal and O_2 molecule. The energy spectrum from SSW-NN structures for each composition is also shown in the color bar. (b) Percentage of different coordinated Co in the GM of CoO_x structures. (c–f) Four representative structures for the GM of CoO_x with the O atomic content (O %) as also indicated in (a). These four GM structures are obtained from SSW-NN search of $\text{Co}_{20}\text{O}_{21}$ (O % = 0.512), $\text{Co}_{20}\text{O}_{22}$ (0.524), $\text{Co}_{20}\text{O}_{24}$ (0.545), and $\text{Co}_{20}\text{O}_{28}$ (0.583) per unit cell. $[\text{CoO}_5]$ and $[\text{CoO}_6]$ indicate the minority five- and six-coordinated Co atoms in structure; v4c indicates the Co vacancy at the tetrahedral site.

reconstructive nature of the phase transition with a large local atomic movement and nonexistence of coherent phase junctions.

We now return to the puzzle on the GM of CoO and the one-way phase transition. Although the theory shows that h-CoO is more stable than c-CoO, experimental evidence appears to favor the opposite: (i) h-CoO can only be obtained in nanocrystals but c-CoO can be synthesized in micro-sized bulky structures; (ii) only the one-way channel from h-CoO to c-CoO transition is found in experiments, which occurs at high temperatures and in vacuum. It was thus believed that h-CoO is a kinetically controlled metastable phase. This puzzle between theory and experiment may be caused by a number of possible reasons, in particular, the intrinsic inaccuracy of DFT as suggested by Saritas et al.⁴⁰

From our results, we expect that the high barrier of solid-to-solid phase transition and the different abilities to adopt defects in two phases may also be a reason of the one-way h-CoO to c-CoO transition. We have already shown that the solid-phase transition in between c-CoO and h-CoO belongs to the reconstructive transition involving Co–O bond breaking and thus requires a high reaction temperature. At high temperatures (i.e., 320 °C in the experiment) where the phase transition can occur, structural defects will inevitably form in CoO crystals, as shown in the global PES, where the high-energy phases just above the c-CoO and h-CoO crystals involve five-coordinated Co, $[\text{CoO}_5]$. These defective phases are mainly c-CoO-like structures because of the poor stability of $[\text{CoO}_3]$ defects in h-CoO. Quantitatively, we found that the presence of structural defects in CoO can help to smooth the difference between h-CoO and c-CoO: in a $\text{Co}_{32}\text{O}_{32}$ unit cell for c-CoO, a defective structure of c-CoO with an O vacancy is 4.37 meV more stable than the defective h-CoO; the defective structure $\text{Co}_{31}\text{O}_{31}$ of c-CoO in Schottky style becomes only 3.21 meV/atom (AFM) less stable than the defective h-CoO. Once the phase transition from h-CoO to c-CoO takes place, as it is a reconstructive phase transition, the reaction must involve the generation of defects, which further drives the one-way reaction. The presence of

defects, either Schottky defects or Frenkel defects, has been reported in the experiment.^{43,44}

3.2. Phase Diagram of CoO_x . Not limited to CoO, we have investigated other CoO_x structures using the SSW-NN method following the same procedure (see Supporting Information Section 1.1.c). To cover the common Co oxidation states including both Co^{2+} and Co^{3+} , our simulation contains a Co atom number ranging from 8 to 24 per unit cell with the oxygen atomic content (O %) ranging from 0.49 to 0.60 (i.e., O/Co ratio ranging from 0.95 to 1.5).

Figure 3a plots the thermodynamic convex hull for CoO_x , where the relative formation energy (ΔE) of CoO_x is with respect to Co metal (hcp) and O_2 molecule. It is obvious that the diagram has two convex points at O % = 1/2 and 4/7 corresponding to the two common phases CoO and Co_3O_4 , respectively. Interestingly, for O % in between 1/2 and 4/7, as CoO_x goes from CoO and Co_3O_4 , all the intermediate phases are thermodynamically highly unstable and the energy maximum appears at about the middle O content, O % = 0.524. This suggests that the phase segregation is highly favored for this intermediate CoO_x (the O content in between 1/2 and 4/7) to become CoO and Co_3O_4 .

Taking all the GM from each composition, we analyzed the evolution of Co coordination with the increase of the O content, as shown in Figure 3b. The proportion of Co atoms with four to six coordination ($[\text{CoO}_4]$, $[\text{CoO}_5]$, and $[\text{CoO}_6]$) at each composition is plotted against the O content. We found that with the increase of O content, the proportion of $[\text{CoO}_4]$ first decreases rapidly from O % = 0 to 0.545, then remains rather constant at 30% in between O % = 0.56 and 0.59, and drops to zero at O % = 0.6 (Co_2O_3). This is apparently because the h-CoO crystal pattern with 100% $[\text{CoO}_4]$ disappears gradually and, the Co_3O_4 and Co_2O_3 crystal pattern contains 33% and zero $[\text{CoO}_4]$, respectively. On the other hand, the proportion of $[\text{CoO}_6]$ tends to increase gradually. The proportion of $[\text{CoO}_5]$ is generally low in concentration in the GM of CoO_x . In fact, they are always related to the phase junctions and defects in the crystal structure.

For the most stable Co_3O_4 , the predicted GM from SSW-NN is the spinel structure ($Fd\bar{3}m$, #227), which has been well documented by both experiment and theory.^{45,46} Because this structure forms the basic pattern for many other CoO_x , we now highlight the characteristic views shown in Figure 4. Co_3O_4 owns

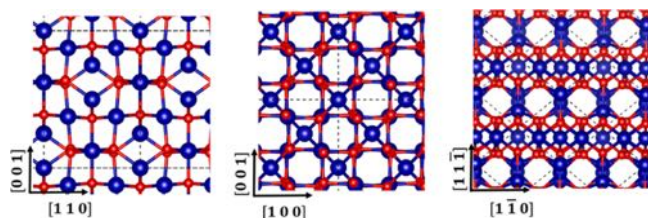


Figure 4. Crystal structure of spinel Co_3O_4 , the most stable phase of CoO_x from global PES.

a cubic closely packed lattice for O anions and Co ions insert into the O fcc sublattice in two different oxidation states, Co^{2+} and Co^{3+} , with a ratio of 1:2. Co^{2+} and Co^{3+} are located in tetrahedral and octahedral interstitial sites, respectively. The Co–O distance is however similar for Co^{2+} and Co^{3+} , ~ 1.93 Å. Compared to the CoO global PES, there are very few low-energy crystal forms in Co_3O_4 , as evident by the discrete energy spectrum above the GM. The second lowest minimum (SLM) has a distorted spinel structure ($C2/m$, #12), 29.9 meV/atom higher in energy. The other two low lying structures are 37.2 meV/atom ($Imma$, #74) and 47.6 meV/atom ($Cmmm$, #65) higher.

For the GM at intermediate O contents, we generally can find the local structural patterns of CoO and Co_3O_4 because of their thermodynamic stability. The GM for O % from 0.512 to 0.545 adopts the defected form or the junction of the three important phases, h-CoO, c-CoO, and Co_3O_4 . Some minority phase pattern appears at the junction region, including CoO_2 (MoS_2 -type structure) and CoO (graphene-type structure). Above O % 0.545, the major phase pattern is the spinel Co_3O_4 phase with either Co or O defects. The four representative compositions, that is, $\text{CoO}_{1.05}$, $\text{CoO}_{1.1}$, $\text{CoO}_{1.2}$, and $\text{CoO}_{1.4}$ are elaborated in the following.

3.2.1. $\text{CoO}_{1.05}$ (O % = 0.512). The GM structure (Figure 3c) is mainly based on the h-CoO structure. The additional oxygen atoms are added into the remaining tetrahedral holes in the h-CoO phase, which form bonds with four neighboring Co atoms and increase the neighboring Co coordination to $[\text{CoO}_5]$. These

newly formed $[\text{CoO}_5]$ tend to segregate as an individual layer in between the closely packed h-CoO(0001), labeled a $[\text{CoO}_5]$ layer, as shown in Figure 3c. This structure has 20% of $[\text{CoO}_5]$ (also see Figure 3b).

3.2.2. $\text{CoO}_{1.1}$ (O % = 0.524). The main framework of the GM (Figure 3d) is basically the h-CoO and twinned h-CoO structure. Similar to $\text{CoO}_{1.05}$, the additional oxygen atoms enter into the tetrahedral holes in the CoO phase. As the number of newly add oxygen atoms increase, the local Co atoms turn into $[\text{CoO}_6]$. This creates a layer of CoO_2 (1T-MoS_2 -type structure) with $[\text{CoO}_6]$. These additional oxygen atoms also distort the original tetrahedra stacking pattern in CoO, fusing two closely packed layers by sharing oxygen atoms to form the $[\text{CoO}_5]$ layers (graphene-type structure). This structure contains 10% $[\text{CoO}_6]$, 20% $[\text{CoO}_5]$, and the remaining 70% $[\text{CoO}_4]$.

3.2.3. $\text{CoO}_{1.2}$ (O % = 0.545). The GM (Figure 3e) is basically a junction structure containing c-CoO and spinel Co_3O_4 phases. The phase junction interface follows the orientation relationship (OR), c-CoO(001)// Co_3O_4 (001) + c-CoO[110]// Co_3O_4 [110]. The cubic side is slightly distorted from the c-CoO with a longer Co–O bond distance (2.28 Å compared to 2.14 Å in c-CoO). On the spinel Co_3O_4 side, the structure contains cobalt vacancy defects near phase junction interface, which are labeled v4c in Figure 3e. Because more oxygen atoms are present compared to CoO, $[\text{CoO}_6]$ becomes the major coordination environment: it has 10% $[\text{CoO}_4]$ and 90% $[\text{CoO}_6]$.

3.2.4. $\text{CoO}_{1.4}$ (O % = 0.583). The GM structure (Figure 3f) is also a phase junction containing c-CoO and defected spinel Co_3O_4 sharing the same OR as described in $\text{CoO}_{1.2}$. The Co_3O_4 part now contains Co vacancies, missing both $[\text{CoO}_4]$ and $[\text{CoO}_6]$ near the phase junction interface. This structure has 70% $[\text{CoO}_6]$ and 30% $[\text{CoO}_4]$.

The above results show that c-CoO and spinel Co_3O_4 can form the stable phase junction, while no coherent interface between h-CoO and Co_3O_4 are found. Because the tendency of segregation for CoO_x at the intermediate composition (O %: 1/2–4/7) is predicted by the thermodynamic convex hull, it is expected that the coexistence of c-CoO and spinel Co_3O_4 is likely over a wide range of O contents. Indeed, an experiment by Senecal et al. has observed c-CoO and spinel Co_3O_4 under the reaction condition of Fischer–Tropsch synthesis.² In addition, we found that in the stable CoO– Co_3O_4 structures, $[\text{CoO}_5]$ can only appear near the O vacancy and are therefore in low concentration. For O % content above 0.575 where Co vacancy

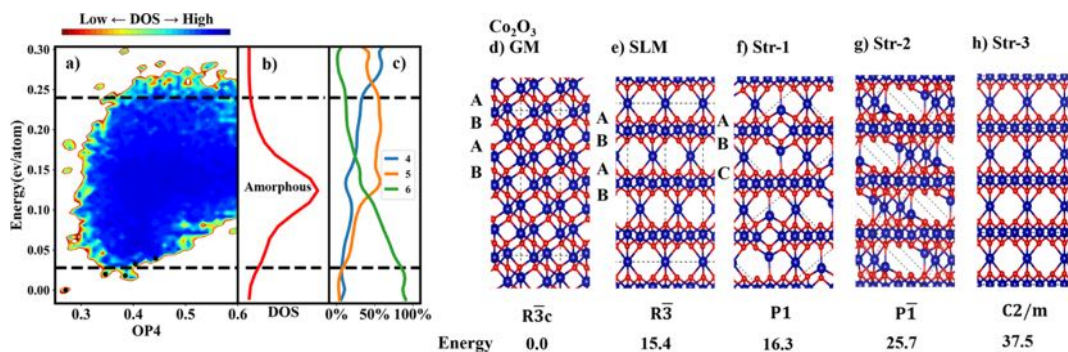


Figure 5. (a–c) Global PES contour plot for Co_2O_3 using minima from SSW-NN, the DOS, and the coordination distribution (see Figure 1 caption for details). (d–h) Five representative structures for Co_2O_3 phases together with the PBE + U relative energy (meV/atom). These structures are also indicated by black dots in (a) with the coordinate (OP_4 , $E(\text{NN})$) as follows: Co_2O_3 -GM (0.27, 0.000); Co_2O_3 -SLM (0.40, 0.017); Co_2O_3 -Str1 (0.38, 0.019); Co_2O_3 -Str2 (0.44, 0.034); and Co_2O_3 -Str3 (0.38, 0.039).

is present, there is no $[\text{CoO}_5]$ in the GM structures. This confirms the fact that $[\text{CoO}_5]$ is not observed in experiments. Our findings on the h-CoO to c-CoO phase transition pathway and the presence of stable phase junction between c-CoO and spinel Co_3O_4 can also explain the experimental fact by Liu et al. that h-CoO will undergo a phase transition into c-CoO first before the final oxidation into Co_3O_4 .⁵

3.3. Global PES of Co_2O_3 . Finally, we focus on Co_2O_3 because its structure remains controversial in experiments. From SSW-NN simulation, we collect 23 170 distinct minima and show them in the global PES Figure 5a, where the energy of Co_2O_3 phases is plotted against the distance-weighted Steinhart-order parameter with degree $l = 4$ (OP_4). Figure 5d–h shows five typical structures of Co_2O_3 , including the GM and the SLM.

We find that the most stable structure for Co_2O_3 phase (Figure 5d) is an $\alpha\text{-Al}_2\text{O}_3$ -like crystal composed by only $[\text{CoO}_6]$ octahedra, each sharing two oxygen atoms with others. The O sublattice has a hexagonal close-packing lattice (ABAB packing) and the Co atoms distribute evenly in between different oxygen close-packing layers.

The SLM, 15.4 meV/atom above the GM, has a crystal structure similar to GM, but with a reduced symmetry ($R\bar{3}$) owing to the Co cation redistribution. In SLM, the octahedra Co atoms have an uneven distribution in the hcp O sublattice: 25% in between the AB layer and 75% in between the BA layer (see Figure 5e). In fact, there are other minima that have similar energy to SLM, as shown in Figure 5f, $\text{Co}_2\text{O}_3\text{-Str-1}$, which, being different from GM and SLM, has an fcc O sublattice. In the structure, the Co cations also distribute unevenly in the fcc O sublattice: 66% Co in between AB layer with $[\text{CoO}_6]$, 17% Co with $[\text{CoO}_6]$, and 17% Co with $[\text{CoO}_4]$ in between the BC layer. It is important to notice that the energy gap between the GM and the SLM in Co_2O_3 is quite large (15.4 meV/atom), if compared that with CoO (h-CoO and f-CoO, 3.3 meV/atom).

Leaving from the SLM, the Co_2O_3 PES enters into the amorphous zone above 0.03 eV/atom. There are a tremendous number of possible minima on the PES, which exhibits a large DOS, as shown in Figure 5b. For the low-energy amorphous structure (Figure 5g–h), they generally maintain the fcc closely packed O sublattice, but the Co positions become disordered. As a result, these structures can be viewed as the packing of the layered 1T-MoS₂-type CoO_2 via the interstitial $[\text{CoO}_4]$ and $[\text{CoO}_6]$ connections. For the higher-energy amorphous structures, we can identify the O–O bond formation, for example, at 0.066 eV/atom higher than the GM, indicating the highly oxidative ability of Co_2O_3 .

Figure 5c shows the change of Co coordination with respect to the energy of Co_2O_3 phases. We found that in the low-energy zone where the crystal structures dominate, $[\text{CoO}_6]$ are the major coordination, indicating that Co^{3+} always prefers the octahedra configuration regardless of the crystal forms. $[\text{CoO}_5]$ are the dominant coordination in the amorphous zone and $[\text{CoO}_4]$ has a large proportion only at very high energy regions (above 0.25 eV/atom).

With these PES data, we can now answer some important puzzles on Co_2O_3 . The difficulty to synthesize trivalent Co_2O_3 crystal might be due to two reasons. First, the GM of Co_2O_3 can be well defined energetically from the global PES, but the SLM is also kinetically stable. The large energy gap between the GM and the SLM suggests the high stability of GM compared to the other crystal forms. The kinetic stability of both GM and SLM has also been verified by computing the solid-phase transition pathway between the GM and the SLM. The potential energy profile and

reaction snapshots of the lowest energy pathway are shown in Supporting Information Figure S5. The reaction has a high barrier of 113.7 meV/atom, which is comparable with that for the h-CoO to c-CoO phase transition.

Second, there is an intrinsic tendency to decompose Co_2O_3 into Co_3O_4 and O_2 at finite temperatures. From the convex hull in Figure 3, we can find that the Co_2O_3 ($\text{CoO}_{1.5}$) and its nearby compositions, that is, $\text{CoO}_{1.4}$, $\text{CoO}_{1.45}$, have nearly the same energy (all on the convex line) for the reaction energy change of $\text{CoO}_x \rightarrow 1/3\text{Co}_3\text{O}_4 + (1/2x - 2/3)\text{O}_2$. In particular, the energy change to decompose the GM of Co_2O_3 is already slightly exothermic by 0.098 eV per Co (0 K) and becomes highly exothermic at finite temperatures. The ease to form O–O species in CoO_x with the O content above 3/7 is evident from the global PES data. For example, the GM for $\text{CoO}_{1.45}$ in $\text{Co}_{20}\text{O}_{29}$ unit cell contains the O–O species together with the spinel pattern of Co_3O_4 . The amorphous structures in Co_2O_3 also have the O–O species in the lattice. Experimentally, Co_2O_3 can be synthesized under high pressure (90 kbar) and high temperature (1000 °C),¹⁰ which can thus be rationalized as the consequence of thermodynamics, where the O_2 is squeezed into solid, forming stable Co_2O_3 at high pressures.

4. CONCLUSIONS

This work represents a comprehensive survey on CoO_x structures, thermodynamic stability, and phase transition pathways by visiting the global PES of CoO_x at different compositions. This formidable task can now be vastly speeded up by using the machine learning method, where the SSW global optimization in combination with G-NN potential produces the global PES data with a low cost. Some key results are highlighted as follows.

- (i) The G-NN potential for CoO_x is established by learning 42 246 first-principles data set, which can describe different CoO_x structures with variable compositions, in particular, bulk structures. The potential is available from the LASP code project (www.lasphub.com).
- (ii) Co_3O_4 and CoO are the only two thermodynamically stable phases according to the calculated CoO_x phase diagram. The difficulty to synthesize trivalent Co_2O_3 crystal is due to both the high kinetic stability of SLM and the tendency of Co_2O_3 decomposition to Co_3O_4 and O_2 at finite temperatures. Co or O vacancies in Co_3O_4 lattice are common features for CoO_x with the O content larger than 0.54.
- (iii) The h-CoO to c-CoO solid phase transition belongs to the reconstructive transition, that is, non-martensitic and having no coherent interface. The phase transition has a high barrier and thus occurs at high temperatures. The preference for structural defects inside c-CoO could be the key factor that leads to the one-way phase transition from h-CoO to c-CoO.
- (iv) Co_3O_4 and c-CoO can achieve the coherent interface to form a stable heterophase junction, which suggests that the phase transition is feasible via O anion diffusion.

■ ASSOCIATED CONTENT

Supporting Information

The Supporting Information is available free of charge on the ACS Publications website at DOI: 10.1021/acs.jpcc.9b02842.

Methodology and calculation details (SSW-NN method, pathway sampling and TS locating, DFT energetics

calculations, the sensitivity analysis of U in GGA + U calculation, the definition of distance-weighted Steinhart-order parameter, and phase diagram thermodynamics analysis); band structure of h-CoO and c-CoO; representative structure on CoO PES; energy and geometry on h-CoO to c-CoO pathway; energy of Co₂O₃ distinct minima; phase transition pathway of Co₂O₃ GM and SLM; optimized XYZ position for h-CoO, c-CoO, and TS on h-CoO to c-CoO transition pathway, GM and SLM of Co₂O₃, and other important CoO_x including CoO_{1.05}, CoO_{1.1}, CoO_{1.2}, and CoO_{1.4} (PDF)

AUTHOR INFORMATION

Corresponding Author

*E-mail: zpliu@fudan.edu.cn.

ORCID

Ye-Fei Li: 0000-0003-4433-7433

Cheng Shang: 0000-0001-7486-1514

Zhi-Pan Liu: 0000-0002-2906-5217

Notes

The authors declare no competing financial interest.

ACKNOWLEDGMENTS

This work was supported by the National Key Research and Development Program of China (2018YFA0208600), National Science Foundation of China (21533001, 91745201, 91645201, and 21603035), the Science and Technology Commission of Shanghai Municipality (08DZ2270500), and Shanghai Pujiang Program (16PJ1401200).

REFERENCES

- (1) Cats, K. H.; Andrews, J. C.; Stéphan, O.; March, K.; Karunakaran, C.; Meirer, F.; de Groot, F. M. F.; Weckhuysen, B. M. Active phase distribution changes within a catalyst particle during Fischer-Tropsch synthesis as revealed by multi-scale microscopy. *Catal. Sci. Technol.* **2016**, *6*, 4438–4449.
- (2) Senecal, P.; Jacques, S. D. M.; Di Michiel, M.; Kimber, S. A. J.; Vamvakeros, A.; Odarchenko, Y.; Lezcano-Gonzalez, I.; Paterson, J.; Ferguson, E.; Beale, A. M. Real-Time Scattering-Contrast Imaging of a Supported Cobalt-Based Catalyst Body during Activation and Fischer-Tropsch Synthesis Revealing Spatial Dependence of Particle Size and Phase on Catalytic Properties. *ACS Catal.* **2017**, *7*, 2284–2293.
- (3) Tsakoumis, N. E.; Walmsley, J. C.; Rønning, M.; van Beek, W.; Rytter, E.; Holmen, A. Evaluation of Reoxidation Thresholds for γ -Al₂O₃-Supported Cobalt Catalysts under Fischer-Tropsch Synthesis Conditions. *J. Am. Chem. Soc.* **2017**, *139*, 3706–3715.
- (4) Risbud, A. S.; Snedeker, L. P.; Elcombe, M. M.; Cheetham, A. K.; Seshadri, R. Wurtzite CoO. *Chem. Mater.* **2005**, *17*, 834–838.
- (5) Nam, K. M.; Shim, J. H.; Han, D.-W.; Kwon, H. S.; Kang, Y.-M.; Li, Y.; Song, H.; Seo, W. S.; Park, J. T. Syntheses and Characterization of Wurtzite CoO, Rocksalt CoO, and Spinel Co₃O₄ Nanocrystals: Their Interconversion and Tuning of Phase and Morphology. *Chem. Mater.* **2010**, *22*, 4446–4454.
- (6) Liu, J. F.; He, Y.; Chen, W.; Zhang, G. Q.; Zeng, Y. W.; Kikegawa, T.; Jiang, J. Z. Bulk Modulus and Structural Phase Transitions of Wurtzite CoO Nanocrystals. *J. Phys. Chem. C* **2007**, *111*, 2–5.
- (7) Khoshandam, B.; Jamshidi, E.; Kumar, R. V. Reduction of Cobalt Oxide with Methane. *Metall. Mater. Trans. B* **2004**, *35*, 825–828.
- (8) Gupta, R. K.; Sinha, A. K.; Raja Sekhar, B. N.; Srivastava, A. K.; Singh, G.; Deb, S. K. Synthesis and Characterization of Various Phases of Cobalt Oxide Nanoparticles Using Inorganic Precursor. *Appl. Phys. A* **2011**, *103*, 13–19.
- (9) Nishi, T.; Hayasaka, Y.; Suzuki, T. M.; Sato, S.; Isomura, N.; Takahashi, N.; Kosaka, S.; Nakamura, T.; Sato, S.; Morikawa, T. Electrochemical Water Oxidation Catalysed by CoO-Co₂O₃-(OH)₂ Multiphase-Nanoparticles Prepared by Femtosecond Laser Ablation in Water. *ChemistrySelect* **2018**, *3*, 4979–4984.
- (10) Chenavas, J.; Joubert, J. C.; Marezio, M. Low-spin \rightarrow high-spin state transition in high pressure cobalt sesquioxide. *Solid State Commun.* **1971**, *9*, 1057–1060.
- (11) Huang, S.-D.; Shang, C.; Zhang, X.-J.; Liu, Z.-P. Material Discovery by Combining Stochastic Surface Walking Global Optimization with a Neural Network. *Chem. Sci.* **2017**, *8*, 6327–6337.
- (12) Huang, S.-D.; Shang, C.; Kang, P.-L.; Liu, Z.-P. Atomic Structure of Boron Resolved Using Machine Learning and Global Sampling. *Chem. Sci.* **2018**, *9*, 8644–8655.
- (13) Shang, C.; Liu, Z.-P. Stochastic Surface Walking Method for Structure Prediction and Pathway Searching. *J. Chem. Theory Comput.* **2013**, *9*, 1838–1845.
- (14) Shang, C.; Zhang, X.-J.; Liu, Z.-P. Stochastic Surface Walking Method for Crystal Structure and Phase Transition Pathway Prediction. *Phys. Chem. Chem. Phys.* **2014**, *16*, 17845–17856.
- (15) Huang, S.-D.; Shang, C.; Kang, P.-L.; Zhang, X.-J.; Liu, Z.-P. Lasp: Fast Global Potential Energy Surface Exploration. *Wiley Interdiscip. Rev.: Comput. Mol. Sci.* **2019**, No. e1415.
- (16) Zhang, X.-J.; Liu, Z.-P. Reaction Sampling and Reactivity Prediction Using the Stochastic Surface Walking Method. *Phys. Chem. Chem. Phys.* **2015**, *17*, 2757–2769.
- (17) Zhang, X.-J.; Shang, C.; Liu, Z.-P. Double-Ended Surface Walking Method for Pathway Building and Transition State Location of Complex Reactions. *J. Chem. Theory Comput.* **2013**, *9*, 5745–5753.
- (18) Kresse, G.; Hafner, J. Ab initio molecular dynamics for liquid metals. *Phys. Rev. B: Condens. Matter Mater. Phys.* **1993**, *47*, 558–561.
- (19) Kresse, G.; Furthmüller, J. Efficiency of Ab-Initio Total Energy Calculations for Metals and Semiconductors Using a Plane-Wave Basis Set. *Comput. Mater. Sci.* **1996**, *6*, 15–50.
- (20) Dirac, P. A. M. Quantum Mechanics of Many-Electron Systems. *Proc. R. Soc. Edinburgh* **1929**, *123*, 714–733.
- (21) Slater, J. C. A Simplification of the Hartree-Fock Method. *Phys. Rev.* **1951**, *81*, 385.
- (22) Perdew, J. P.; Wang, Y. Accurate and Simple Analytic Representation of the Electron-Gas Correlation Energy. *Phys. Rev. B: Condens. Matter Mater. Phys.* **1992**, *45*, 13244.
- (23) Perdew, J. P.; Burke, K.; Ernzerhof, M. Generalized Gradient Approximation Made Simple. *Phys. Rev. Lett.* **1996**, *77*, 3865.
- (24) Perdew, J. P.; Burke, K.; Ernzerhof, M. Generalized Gradient Approximation Made Simple [Phys. Rev. Lett. **77**, 3865 (1996)]. *Phys. Rev. Lett.* **1997**, *78*, 1396.
- (25) Dudarev, S. L.; Botton, G. A.; Savrasov, S. Y.; Humphreys, C. J.; Sutton, A. P. Electron-Energy-Loss Spectra and the Structural Stability of Nickel Oxide: An LSDA+ U Study. *Phys. Rev. B: Condens. Matter Mater. Phys.* **1998**, *57*, 1505–1509.
- (26) Singh, V.; Major, D. T. Electronic Structure and Bonding in Co-Based Single and Mixed Valence Oxides: A Quantum Chemical Perspective. *Inorg. Chem.* **2016**, *55*, 3307–3315.
- (27) García-Mota, M.; Bajdich, M.; Viswanathan, V.; Vojvodic, A.; Bell, A. T.; Nørskov, J. K. Importance of Correlation in Determining Electrocatalytic Oxygen Evolution Activity on Cobalt Oxides. *J. Phys. Chem. C* **2012**, *116*, 21077–21082.
- (28) Wang, L.; Maxisch, T.; Ceder, G. Oxidation Energies of Transition Metal Oxides within the GGA+ U Framework. *Phys. Rev. B: Condens. Matter Mater. Phys.* **2006**, *73*, 195107.
- (29) Krukau, A. V.; Vydrov, O. A.; Izmaylov, A. F.; Scuseria, G. E. Influence of the Exchange Screening Parameter on the Performance of Screened Hybrid Functionals. *J. Chem. Phys.* **2006**, *125*, 224106.
- (30) Jauch, W.; Reehuis, M.; Bleif, H. J.; Kubanek, F.; Pattison, P. Crystallographic Symmetry and Magnetic Structure of CoO. *Phys. Rev. B: Condens. Matter Mater. Phys.* **2001**, *64*, 052102.
- (31) Kitaev, Y. E.; Tronc, P. Ferromagnetic and Antiferromagnetic Ordering in the Wurtzite-Type Diluted Magnetic Semiconductors. *Phys. Solid State* **2012**, *54*, 520–530.
- (32) Garza, A. J.; Scuseria, G. E. Predicting Band Gaps with Hybrid Density Functionals. *J. Phys. Chem. Lett.* **2016**, *7*, 4165–4170.

- (33) Wang, Y.; Ge, H. X.; Chen, Y. P.; Meng, X. Y.; Ghanbaja, J.; Horwat, D.; Pierson, J. F. Wurtzite CoO: A Direct Band Gap Oxide Suitable for a Photovoltaic Absorber. *Chem. Commun.* **2018**, *54*, 13949–13952.
- (34) Jain, A.; Hautier, G.; Ong, S. P.; Moore, C. J.; Fischer, C. C.; Persson, K. A.; Ceder, G. Formation Enthalpies by Mixing GGA and GGA + U Calculations. *Phys. Rev. B: Condens. Matter Mater. Phys.* **2011**, *84*, 045115.
- (35) Dean, J. A. *Lange's Handbook of Chemistry*; McGraw-Hill, Inc.: London, 1999.
- (36) Zhang, X.-J.; Shang, C.; Liu, Z.-P. Pressure-Induced Silica Quartz Amorphization Studied by Iterative Stochastic Surface Walking Reaction Sampling. *Phys. Chem. Chem. Phys.* **2017**, *19*, 4725–4733.
- (37) Navrotsky, A.; Muan, A. Activity-composition relations in the systems CoO–ZnO and NiO–ZnO at 1050°C. *J. Inorg. Nucl. Chem.* **1971**, *33*, 35–47.
- (38) DiCarlo, J.; Navrotsky, A. Energetics of Cobalt(II) Oxide with the Zinc-Blende Structure. *J. Am. Ceram. Soc.* **1993**, *76*, 2465–2467.
- (39) Meyer, W.; Hock, D.; Biedermann, K.; Gubo, M.; Müller, S.; Hammer, L.; Heinz, K. Coexistence of Rocksalt and Wurtzite Structure in Nanosized CoO Films. *Phys. Rev. Lett.* **2008**, *101*, 016103.
- (40) Saritas, K.; Krogel, J. T.; Reboredo, F. A. Relative Energies and Electronic Structures of CoO Polymorphs through Ab Initio Diffusion Quantum Monte Carlo. *Phys. Rev. B* **2018**, *98*, 155130.
- (41) Liu, J. F.; He, Y.; Chen, W.; Zhang, G. Q.; Zeng, Y. W.; Kikegawa, T.; Jiang, J. Z. Bulk Modulus and Structural Phase Transitions of Wurtzite CoO Nanocrystals. *J. Phys. Chem. C* **2007**, *111*, 2–5.
- (42) Liu, J. F.; Yin, S.; Wu, H. P.; Zeng, Y. W.; Hu, X. R.; Wang, Y. W.; Lv, G. L.; Jiang, J. Z. Wurtzite-to-Rocksalt Structural Transformation in Nanocrystalline CoO. *J. Phys. Chem. B* **2006**, *110*, 21588–21592.
- (43) Chen, W. K.; Jackson, R. A. Oxygen Self-Diffusion in Undoped and Doped Cobaltous Oxide. *J. Phys. Chem. Solids* **1969**, *30*, 1309–1314.
- (44) Fryt, E. Defect Structure in CoO. *Oxid. Met.* **1976**, *10*, 311–327.
- (45) Smith, W. L.; Hobson, A. D. The Structure of Cobalt Oxide, Co₃O₄. *Acta Crystallogr., Sect. B: Struct. Crystallogr. Cryst. Chem.* **1973**, *29*, 362–363.
- (46) Chen, J.; Wu, X.; Selloni, A. Electronic Structure and Bonding Properties of Cobalt Oxide in the Spinel Structure. *Phys. Rev. B: Condens. Matter Mater. Phys.* **2011**, *83*, 245204.